Fast Horizon Computation for Accurate Terrain Rendering

A. James Stewart *

Technical Report 349
Department of Computer Science
University of Toronto
June 1996

Abstract

To render a terrain that is represented by many sample points, we must determine what part of the sky is visible from each sample point. The direct primary illumination of each point can then be computed for any distribution of sky illumination.

This paper presents an efficient and practical method to compute the horizon, or skyline, at all sample points on a terrain. For a large terrain of 915,800 points, the horizon computation takes only 2.9 hours.

From the horizons, the radiosity of each point can be determined in two ways: either *quickly*, using an approximate lighting model that relies upon only the direct primary illuminations, or *accurately*, with a progressive radiosity algorithm that uses the direct primary illuminations as the initial point irradiances, for a considerable savings in time.

The new horizon computation method is compared with another method by Cabral, Max, and Springmeyer. Experimental results are reported which show that the new method yields more accurate rendered images and takes much less time to process large terrains.

Key Phrases: terrain rendering, horizon, skyline, shading, radiosity

Additional images and animations for this paper are available at
`http://www.dgp.toronto.edu/people/JamesStewart`

*Dynamic Graphics Project, Department of Computer Science, University of Toronto, 10 Kings College Road, Toronto, Ontario, Canada, M5S 1A4. phone: (416) 978–5359. fax: (416) 978–5184. email: jstewart@cs.toronto.edu

1 Introduction

Terrain rendering is used in scientific visualization, flight simulation, bump mapping, and cartographic applications. For example, otherwise unobtainable views from the surface of Mars have been generated from terrain data [Cap].

To render a terrain that is represented by many sample points, we must compute the total light received by each sample point (its irradiance) in order to determine how much is emitted (its radiosity). The largest contribution to the irradiance of a sample point comes from the sky, although smaller contributions come from other surfaces of the terrain.

To determine the direct primary illumination from the sky, it is necessary to determine the boundary, or horizon, of the visible sky. Once the horizon is computed for each sample point, we can quickly compute the direct primary illumination of each point for *any* distribution of sky light. As shown in Section 6, the direct primary illumination is sufficient to render realistic and informative images without resorting to an expensive radiosity step. However, if a progressive radiosity computation is desired, the horizon method provides the important initial irradiance of each point, which will speed up the radiosity computation considerably.

This paper describes how to compute efficiently the horizon at every sample point of a terrain. The method has been implemented and tested on terrains of up to $915,800$ points, the largest available to the author. On the largest terrain, the method took 2.9 hours, which compares quite favorably to two other methods (described in the next section) which took 7.2 hours and 33 days, respectively.

Images have been generated using an approximate illumination model [SL95] that requires only the direct primary illumination. From the horizon information, the radiosity of the sample points can be computed using this model at a rate of 3600 points per second for a discretized distribution of sky illumination.

2 Background

Closely related work has been done by Max [Max88], who computes horizons for bump–mapped surfaces. He considers eight directions around each sample point and determines the horizon elevation in each direction. Points that do not fall directly in the eight directions are not considered in determining the horizon. When rendering, a sample point is considered to be illuminated if the sun is visible from the point, which is determined by comparing the sun's elevation with the closest known horizon elevation. Intensity within penumbral shadows is determined according to the fraction of the sun's disc that lies above the horizon. Supersampling on pixels is performed to diminish aliasing artifacts. Max also describes transformations of bump maps to curved surface patches.

The method presented in this paper differs significantly from that of Max. In building each horizon, we consider all sample points of the terrain, rather than only those that lie in particular directions. This results in more accurate horizons and, hence, more accurate terrain rendering. It also enables us to produce soft shadows under nonuniform diffuse illumination. As Max states, his approach is not well suited to casting shadows from bumpy profiles, since this requires a much denser sampling of horizon elevations. In addition, terrains with sharp spikes will result in undersampling artifacts (like absent shadows) with his method. By considering *all* points of the terrain when building each horizon, we avoid these problems. However, considering all points for each horizon can be extremely expensive. Our goal is to do this quickly when the number of points is very large.

Horizon maps like those of Max are used by Cabral, Max, and Springmeyer [CMS87] to compute bidirectional reflection functions for bump maps. They use 24 directions around each point and sample a triangulated terrain instead of discrete points. This is a more accurate and slightly more expensive procedure which reduces — but does not eliminate — undersampling artifacts. This will be called the *CMS* approach. In Section 5, we compare the performance of CMS to the approach presented in this paper.

Shaded terrains have also been generated using shadow volumes (for example, Kaneda *et al* [KKN+89]) and ray tracing (for example, Coquillart and Gangnet [CG84]). Shadow volumes only apply to point light sources, and ray tracing can be expensive if sampling is used to incorporate diffuse illumination [Kaj86].

Related work on terrains appears in the computational geometry literature. If the terrain is modelled as a polygonal mesh on n points, computing the horizon for a *single* point is equivalent to computing the upper envelope of a set of $\mathcal{O}(n)$ segments [Ata83]. The horizon has complexity $\mathcal{O}(n\ \alpha(n))$ [1] and can be computed in optimal time $\mathcal{O}(n \log n)$ [Her89]. Alternatively, a hierarchical model can be used to represent the surface at various resolutions [DP88, SP90, dBD95]. In this model, the horizon can be computed for a single point at different resolutions in time $\mathcal{O}(n \log n)$ [DM95].

[1] $\alpha(n)$ is the extremely slowly growing inverse of Ackermann's function, and can be considered constant for any practical n.

2.1 Approximate Horizons

For accurate rendering, the horizon must be determined at each of the n sample points. It is not clear how any of the results described above can be extended to compute the horizon at each of n points in subquadratic total time, or whether this is even possible when each horizon is represented as a polygonal chain of size $\mathcal{O}(n\ \alpha(n))$.

To achieve subquadratic running time, we approximate the horizon of each sample point: The horizon is divided into s sectors, each spanning $\frac{2\pi}{s}$ radians. In each sector, the horizon is assumed to have constant elevation, which is the maximum of the elevations of *all* the sample points that appear in the sector. The user can choose s to control the accuracy of the approximation.

The methods of Max [Max88] and of Cabral, Max, and Springmeyer [CMS87] can also be thought of as constructing the approximate horizon: Each method divides the horizon into a number of sectors and, in each sector, determines the elevation of the horizon by sampling only those terrain points or terrain edges that fall on the *centreline* of the sector.

Consider a terrain consisting of a single, tall, narrow spike. It is clear that these two methods will miss the spike if it does not fall exactly on the centreline of a sector, which will result in a missing shadow. However, the approach taken by this paper will use the narrow spike to define the horizon of the entire sector, which may be much wider than the spike. This might cause shadows to appear where they should not. In Section 6 we will demonstrate that the undersampling artifacts of the first two methods are more severe than the artifacts produced by the new method.

The approximate horizons at each of n points can be computed in a straightforward manner in $\mathcal{O}(n^2)$ time, as follows: For each point p, consider each other point q. Determine which sector of p contains q and store in that sector the elevation of q if it is greater than the maximum elevation stored so far. Such an algorithm is exorbitantly expensive for even moderately sized terrains: The author's implementation took 9.5 hours on a $100,000$–point terrain and would have taken 792 hours (i.e. 33 days) on a $915,800$–point terrain if run to completion.

Note that other, more complicated, algorithms that treat each point individually will be even slower (for example, [Her89] and [DM95] would run in $\mathcal{O}(n^2 \log n)$ time). However, the sampling methods of Max [Max88] and Cabral, Max, and Springmeyer [CMS87] only take time $\mathcal{O}(n^{1.5})$ (each of the n points must consider $\mathcal{O}(\sqrt{n})$ other points in a fixed number of directions around it).

This paper presents a much faster algorithm to compute the approximate horizon at each of n points in total time $\mathcal{O}(s\ n \log^2 n)$ and space $\mathcal{O}(n \log n)$. The algorithm is not difficult to implement: It took the author less than a week. The most complicated operations required are to insert a point into a convex hull and to compute a tangent from a point to a convex hull. Experimental results in Section 5 show that, as the number of points increases, the new algorithm's execution time grows much more slowly than that of the CMS algorithm. Thus, the new algorithm is better suited for very large terrains.

The next two sections describe the horizon computation algorithm. Following that, implementation results and rendered images are presented.

3 Preliminaries

The input consists of a set of n sample points $p_1, \ldots, p_n$, where p_i has coordinates (x_i, y_i, z_i); coordinate z_i is the height of the point. No two points project to the same location in the x–y plane. It is not necessary that the points lie on a regular (x_i, y_i) grid.

Refer to Figure 1 for the following definitions. Throughout this discussion, a vertical direction is parallel to the z axis and a horizontal direction is parallel to the x–y plane. The positive z direction is "up."

The **azimuth angle** of a vector v in $\Re^3$ is the angle of the projection of v onto the x–y plane, measured counterclockwise from the positive x axis when viewed from above. The space around a point p is divided into s regions based on azimuth angle: The **sector σ_i of a point** p is the region of $\Re^3$ reachable from p by (non–vertical) vectors having azimuth angle in the closed range $[\ \frac{2\pi}{s}\ i, \frac{2\pi}{s}\ (i+1)\ ]$.

Let π_i be the vertical plane that bisects the sector σ_i of the origin (that is, the azimuth angle of any non–vertical vector in π_i will be $\frac{2\pi}{s}\ (i + \frac{1}{2})$ (modulo π). Let r_i be a horizontal vector pointing in the direction $\frac{2\pi}{s}\ (i + \frac{1}{2})$. Let the notation $\hat{v}_i$ denote the projection of a vector v onto π_i.

The **elevation angle** of a point q that falls within sector σ_i of a point p is the angle between r_i and the projection $\widehat{pq}_i$ of the vector pq (see angle Θ in Figure 1). The angle has the same sign as the z component of $\widehat{pq}_i$. This definition is slightly different from the usual one and is necessary in the algorithm that follows. Finally, the **approximate horizon** of a point p is a sequence $e_0, \ldots, e_{s-1}$ of s elevation angles, where e_i is the maximum of the elevations of the points that fall within sector σ_i of p. In this model, the horizon is a piecewise–constant function of azimuth angle.

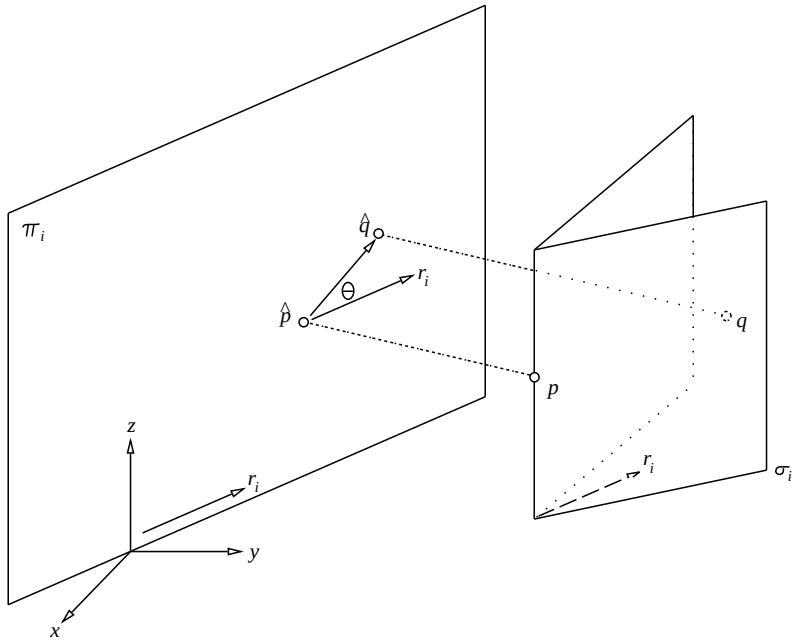

Figure 1: Shown is a point p of the terrain and the sector σ_i of p; point q falls within the sector. The horizontal vector r_i bisects the sector and is parallel to the plane π_i, which passes through the origin. The projections of p and q onto π_i are denoted $\hat{p}$ and $\hat{q}$, respectively. The elevation angle of q in sector σ_i of p is denoted Θ.

4 The Algorithm

The algorithm iterates over the s sectors. Each sector is treated independently (in effect, the algorithm starts anew for each sector). In the i^{th} iteration, the maximum elevation e_i in sector σ_i is calculated for each of the n terrain points.

For a particular point p, this is accomplished as follows. All terrain points q_j that fall within sector σ_i of p are projected onto points $\widehat{q_j}_i$ in the plane π_i. A **covering set** of $\mathcal{O}(\log n)$ upper convex hulls[2] is built whose union contains all of the points $\widehat{q_j}_i$ (see Figure 2). The tangent between $\hat{p}$ and each of the upper hulls is computed in $\mathcal{O}(\log n)$ time per tangent [OvL81]. The elevation of the highest tangent is recorded in e_i. Given the covering set of upper hulls, this procedure takes $\mathcal{O}(\log^2 n)$ time per terrain point per sector. It remains to efficiently construct the covering sets.

Refer to Figure 3 for the following definitions. We will "transform" the sample points from an x–y–z coordinate system to an $a^\perp$–$b^\perp$–z coordinate system in which the sector boundaries are perpendicular to the $a^\perp$ and $b^\perp$ axes. Let a be a horizontal vector in the direction $\frac{2\pi}{s}\ i$ and let b be a horizontal vector in the direction $\frac{2\pi}{s}\ (i+1)$. These vectors define the extreme directions of the sector σ_i. Let $a^\perp$ be a horizontal vector $\frac{\pi}{2}$ radians clockwise of a. Similarly, let $b^\perp$ be a horizontal vector $\frac{\pi}{2}$ radians clockwise of b.

Order the terrain points in the direction $a^\perp$ and let j denote the position of point p in the ordering. Similarly, order the points in the direction $b^\perp$ and let k denote p's position in the ordering. In both orderings, the first point has position 1. For convenience in what follows, we will attach these subscripts to p, as in $p_{j,k}$. Note that one subscript is sufficient to distinguish a point and the notation $p_{j,*}$ or $p_{*,k}$ may be used without ambiguity. Finally, let $\Sigma_{j,k}$ denote sector σ_i of point $p_{j,k}$.

The following observation is exploited to efficiently generate the covering sets. See Figure 3 for an example.

Observation *Point $p_{j,k}$ lies in exactly those sectors $\Sigma_{s,t}$ for which $s > j$ and $t < k$.*

[2] An **upper convex hull**, or simply **upper hull**, is the upper chain of a convex hull with two extreme edges extending vertically downward to $-\infty$. While the hull may contain many points on its interior, we only store the points that define the hull's boundary.

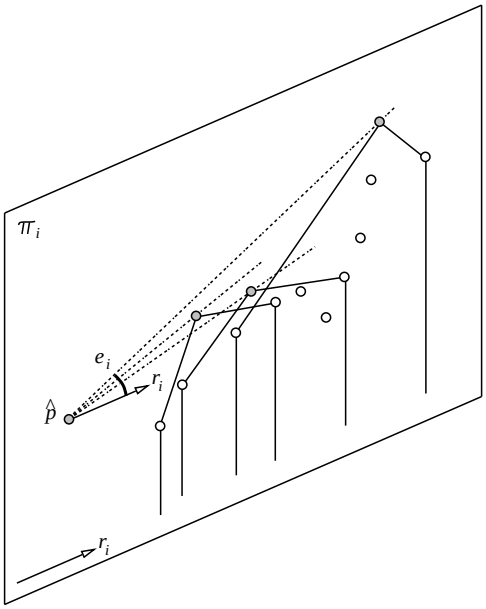

Figure 2: Plane π_i is shown with projection $\hat{p}$ of the point p and projections $\widehat{q_j}_i$ (unlabelled in the figure) of the points q_j that fall within sector σ_i of p. Three upper hulls form a covering set whose union contains all the $\widehat{q_j}_i$. The elevation e_i of the horizon of p is the elevation of the highest of the three tangents from $\hat{p}$ to the upper hulls.

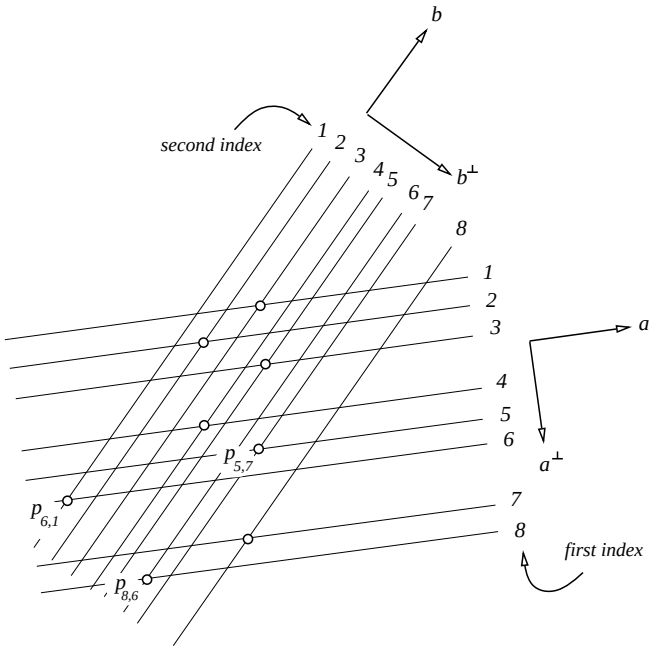

Figure 3: A top view of the terrain points is shown. The sector $\Sigma_{i,j}$ of a terrain point $p_{i,j}$ is the region above and to the right of the point, delimited by the lines passing through the point. According to the Observation, point $p_{5,7}$ lies in exactly the sectors $\Sigma_{6,1}$ and $\Sigma_{8,6}$.

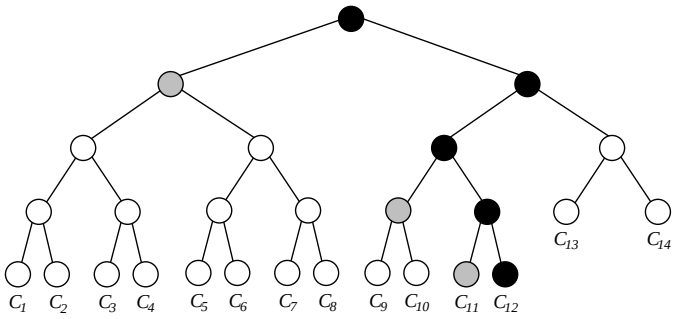

Figure 4: A complete binary tree of upper hulls in which leaf $\mathcal{C}_k$ corresponds to sector $\Sigma_{*,k}$. The covering set of sector $\Sigma_{*,k}$ consists of those upper hulls on the root–to–$\mathcal{C}_k$ path. For example, the black nodes contain the covering set of sector $\Sigma_{*,12}$. To add point $p_{*,12}$ to the covering sets of sectors $\Sigma_{*,1}, \Sigma_{*,2}, \ldots, \Sigma_{*,11}$, it is sufficient to add it to the upper hulls (shown in gray) to the immediate left of the root–to–$\mathcal{C}_{12}$ path.

4.1 Algorithm Description

The algorithm maintains a complete, static, binary tree[3] in which each node stores an upper hull (see Figure 4). The leaf nodes are labelled $\mathcal{C}_1, \ldots, \mathcal{C}_n$ from left to right. The covering set of sector $\Sigma_{*,k}$ consists of the upper hulls stored in the nodes on the root–to–$\mathcal{C}_k$ path, which is of length $\mathcal{O}(\log n)$.

For each sector i, the following is performed: Initially, terrain points are sorted to determine the indices j and k. They are then processed in order of increasing first index, j. Point $p_{j,k}$ is processed as follows:

1. The tangents from $\widehat{p_{j,k}}_i$ (the projection of $p_{j,k}$ onto π_i) to each of the upper hulls on the root–to–$\mathcal{C}_k$ path are computed. The elevation of the highest tangent is recorded as the elevation e_i of the horizon in sector $\Sigma_{j,k}$. As stated above, this takes $\mathcal{O}(\log^2 n)$ time.

2. Point $p_{j,k}$ is added to the covering sets of sectors $\Sigma_{*,1}, \Sigma_{*,2}, \ldots, \Sigma_{*,k-1}$. This is accomplished by inserting $p_{j,k}$ into the upper hull of every left child on the root–to–$\mathcal{C}_k$ path, which is of length $\mathcal{O}(\log n)$ (see Figure 4). Each insertion can be done in time $\mathcal{O}(\log n)$ [PS85] for a total time of $\mathcal{O}(\log^2 n)$.

4.2 Discussion

Recall the Observation. Step 2 adds $p_{j,k}$ to the covering sets of all sectors $\Sigma_{s,t}$ for which $t < k$. Those sectors for which $s > j$ remain to be treated, since sectors are treated in increasing order of first index. Thus, when $p_{s,t}$ is treated, all points $p_{j,k}$ for which $s > j$ and $t < k$ will have been added to the covering set of $\Sigma_{s,t}$. Thus, Step 1 computes the correct elevation e_i.

To reduce space requirements and increase speed, a leaf node $\mathcal{C}_k$ of the tree is marked as **inactive** once the corresponding point $p_{*,k}$ has been processed. The hull associated with the inactive node is discarded, since it is not required after the elevation of $p_{*,k}$ is computed. An internal node is marked as inactive (and its hull discarded) when its two children become inactive. In Step 2 above, $p_{j,k}$ is *not* inserted into inactive hulls.

To reduce space further, note that points are only inserted into hulls of tree nodes that are left children. All right children (and the root) have empty hulls. Thus, only the left children need to be stored, which can be done in a heap–ordered array [CLR90]. This requires a bit of care with array indices when traversing the root–to–$\mathcal{C}_k$ path, but reduces the size of the tree by half. For example, in the author's implementation this saves about 8 megabytes in a terrain of a million points.

The key idea of the algorithm is that a point can be added to the covering sets of sectors $\Sigma_{*,1}, \Sigma_{*,2}, \ldots, \Sigma_{*,k-1}$ by inserting it into only $\mathcal{O}(\log n)$ upper hulls. Since each terrain point can be added to only $\mathcal{O}(\log n)$ upper hulls, the storage bound is clearly $\mathcal{O}(n \log n)$.

Theorem *For a terrain of n data points, the approximate horizon consisting of s sectors can be computed in time $\mathcal{O}(s\, n \log^2 n)$ time and $\mathcal{O}(n \log n)$ space.*

[3] In a complete binary tree, all levels are full except the bottommost, which is filled from left to right. Since the tree is static (it doesn't change shape), it can be stored in an array $A[1 \ldots N]$ such that the two children of node $A[i]$ are $A[2i]$ and $A[2i+1]$.

4.3 Degenerate Situations

Care must be taken with terrain points that fall exactly upon the boundary of a sector; this occurs frequently with grid data. We must ensure that such points are included in the sector; otherwise, we may underestimate the sector elevation. Consider Figure 5. When sorting the points by $a^\perp$ to determine their processing order, points that have the same projection onto $a^\perp$ must be sorted by their projection onto $-a$. This ensures that points lying on the more clockwise boundary of the sector of a point p are processed (and hence added to the sector) before p is processed. When sorting the points by $b^\perp$, points that have the same projection onto $b^\perp$ must be sorted by their projection onto $+b$. This ensures that points lying on the more counterclockwise boundary of the sector of a point p have a larger second index (k) than p, and are thus added to the sector of p when they are processed (recall that a point with second index k is added to the sectors $\Sigma_{*,1}$ to $\Sigma_{*,k-1}$).

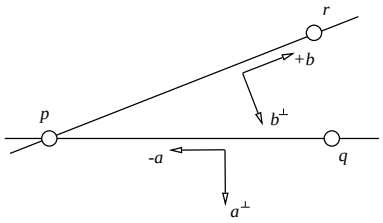

Figure 5: Points q and r fall on the clockwise and counterclockwise boundaries, respectively, of a sector of p. In order that q is stored in the sector, it must be processed before p and so must precede p in the ordering by $a^\perp$. Although r already precedes p in the $a^\perp$ ordering, it must *follow* p in the $b^\perp$ ordering if it is to be stored in p's sector.

4.4 Narrow Sectors

Care must be taken when the sector angle $\frac{2\pi}{s}$ is small. Narrow sectors will often not intersect a terrain point until some distance from the sector vertex. If closer terrain points are higher than the first intersected point, the elevation will be underestimated and, hence, the irradiance will be overestimated (see Figure 6).

The solution is to test the elevations of a fixed number of terrain points that border the sector close to the sector vertex, in addition to determining the maximum elevation of the $\mathcal{O}(\log n)$ upper hulls in the usual way. Suppose that the terrain points are regularly spaced a distance d apart. In the worst case, the sector will not intersect a terrain point until it becomes about this wide. Since the sector has width d at about distance $\frac{d}{\sin(\frac{2\pi}{s})}$ from the vertex, only $\frac{2}{\sin(\frac{2\pi}{s})}$ terrain points bordering the sector must be checked. For large s, $\sin(\frac{2\pi}{s}) \approx \frac{2\pi}{s}$ and the number of bordering points is approximately $\frac{s}{\pi}$.

For example, if 64 sectors are used, only 20 additional terrain points must be checked. As each point takes about 3×10^{-6} seconds to test (which was experimentally determined), this takes only one additional minute for the whole, 915,800–point terrain. This solution is simply an application of the CMS algorithm in a small, bounded area around each point.

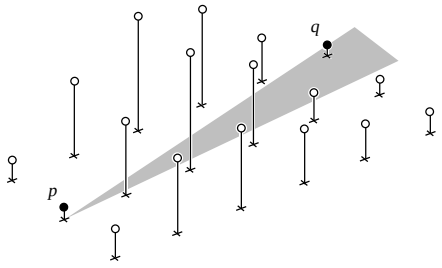

Figure 6: A set of terrain points are shown on top of vertical segments that indicate their heights with respect to the x–y plane. The shaded area of the x–y plane is a sector of p that has its elevation incorrectly determined by point q, the only point to fall within the sector. The elevation should be determined by the high points closer to p.

5 Experimental Results: Running Times

The algorithm was implemented in 1100 lines of C++ code. It was tested on terrains of between 1000 points and 915,800 points, the largest available to the author. Running times on a 166 MHz Pentium PC running Linux with 64 Mb RAM are summarized in Table 1. For comparison, the CMS algorithm was implemented and tested on the same scenes. The straightforward $\mathcal{O}(n^2)$ algorithm, described in Section 2.1, was also implemented and tested on some of the same scenes (its time for the largest scene is extrapolated from the smaller scenes). The algorithms computed horizons of 64 sectors (or 64 sampling directions, in the case of CMS).

Figure 7 shows the running times on a log / log graph (in which the line slopes correspond to the exponents of the algorithm's running times). This graph shows that, *in practice*, the new algorithm exhibits almost linear growth in execution time, while the CMS algorithm exhibits approximately $\mathcal{O}(n^{1.5})$ growth, as expected. The new algorithm clearly outperforms the CMS algorithm as the terrain size increases.

Table 1: Running Times (in seconds)

Terrain Size	New Algorithm	CMS Algorithm	$\mathcal{O}(n^2)$ Algorithm
1,000	5	2	4
3,136	18	6	
10,000	61	24	331
40,000	302	176	
100,000	911	893	34,100
315,844	3,320	5,570	
915,800	10,600	25,800	2,850,000

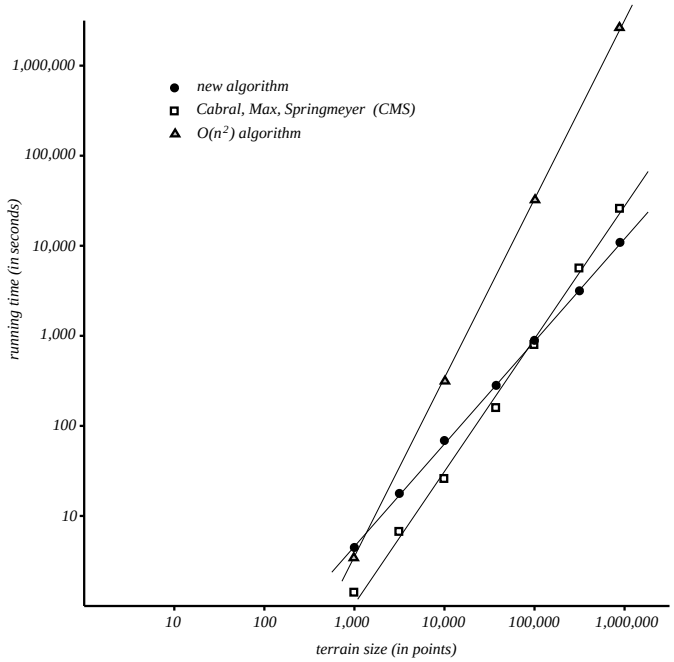

Figure 7: A log / log graph of the running times of the three algorithms. If the line interpolating the results for a particular algorithm has slope k, that algorithm runs in time $\mathcal{O}(n^k)$ on inputs of size n. These experimental results show that the new algorithms runs in time $\mathcal{O}(n^{1.1})$, the CMS algorithm runs in time $\mathcal{O}(n^{1.6})$, and the straightforward algorithm runs in time $\mathcal{O}(n^{2.0})$. This shows that the new algorithm easily outpaces the others, especially as the input gets large. (It's also marvellous that these experimental results correlate so well with the theoretical asymptotic running times.)

Memory requirements are a concern with large terrains. Experiments with the new algorithm show that the average number of points stored in each hull of the binary tree (Section 4.1) was less than two for all terrains tested. Since the average hull size is so small in practice, it is neither necessary nor desirable to use a sophisticated data structure to store the hulls. A simple sorted array for the points of each hull uses very little space and achieves sufficient speed. (In fact, the times reported in Table 1 are for an algorithm that uses a simple sorted array for each hull.) A more sophisticated data structure, like a concatenable queue [PS85], is unnecessary and uses far more space. Using a concatenable queue, the algorithm ran out of memory for the largest terrain.

6 Experimental Results: Rendering Quality

The horizon allows us to compute the direct primary illumination of each terrain point. For accurate rendering, we should also consider reflected illumination that arrives at each point. In this case, the direct primary illuminations computed from the horizons can serve as the initial irradiances for a progressive radiosity algorithm.

6.1 Illumination Model

To avoid the expensive radiosity computation, we will use a global illumination model developed elsewhere [SL95]. This model, which provides a coarser approximation of the radiosity of a point, only considers direct primary illumination. The model exploits the following observation: In a terrain, bright points on peaks tend to see other bright points on peaks, while dark points in valleys tend to see other dark points in valleys. That is, points tend to see other points of approximately the same radiance. Exploiting this observation, we modify the radiosity equation $L(x) = \frac{\rho}{\pi} \int_\Omega L_i(\theta, \phi) \cos\theta \, d\omega$ by replacing the incoming radiance $L_i(\theta, \phi)$ with the point's radiance $L(x)$ in those directions (θ, ϕ) in which the terrain is visible.

We will not discuss further the illumination model, since it is not an issue in this paper: The contribution of this paper is the horizon algorithm. We are simply using the illumination model to produce rendered terrains from the computed horizons.

To model nonuniform sky illumination, the hemisphere of sky directions is discretized into 256 s equal–area regions: Azimuth angle ϕ is divided into s sectors corresponding to the s sectors of the horizon; each sector of the hemisphere is divided by elevation angle θ into 256 equal–area regions. Each region has a constant illumination which is defined by the user.

The radisoity $L(x)$ is computed quickly using lookup tables indexed by horizon elevation and sector. The author's rendering program computes $L(x)$ for about 3600 terrain points per second.

6.2 Rendered Images

Both the new algorithm and the CMS algorithm have problems in terrains with tall, narrow spikes. The CMS algorithm may miss the spikes (generating no shadows at all), while the new algorithm may generate too large a shadow, since it uses the highest point in a sector to define the elevation across the whole sector.

Figure 8 shows a terrain of 100×100 sample points, viewed from directly above. The images in the left column are rendered from horizons computed by the CMS algorithm, while those in the right column are rendered from horizons computed by the new algorithm presented in Section 4. All points have height zero, except a single point in the upper–left corner which has height 50 and represents a tall, narrow spike. The light source is 30 degrees above the horizon and its intensity is modelled as $\cos^{100}\theta$, where θ is the angle between the view direction and the source direction.[4] This models (very roughly) the atmospheric diffusion of illumination that occurs on a clear day.

On the top row of Figure 8, 125 sampling directions were used for the CMS algorithm, while 64 sectors were used for the new algorithm. On the bottom row, 250 sampling directions and 250 sectors were used.

On the top row, the difference in the number of sampling directions (CMS algorithm) and sectors (new algorithm) resulted in equal execution times and, hopefully, a fair comparison. Note, however, that the execution time of the CMS algorithm increases much more quickly than that of the new algorithm as the terrain size increases. For large terrains, we would have to use *fewer* sampling directions than sectors to maintain equal running times.

In the upper–left image of Figure 8, the CMS sampling directions are clearly visible: Terrain points that see the spike in one of the sampling directions are darker than their immediate neighbours that do not see the spike. This is a perceptually disquieting artifact (it seems to imply the existence of multiple light sources) and can be avoided with a denser sampling.

[4] Due to the coarse discretization of the hemisphere of sky directions, the light source occupied a significant area of the sky and caused a large penumbral area.

In the upper–right image, the shadows are softer, as one would expect from a diffuse area source. The sector directions are evident, although the (unbiased?) author finds the artifacts less disquieting than those in the upper–left image. Note the variation of intensity across each sector in the upper–right image. In each sector, the radial position of the highest point in that sector is stored. This allows us to perform linear interpolation of horizon elevation between adjacent sectors. To be fair, this interpolation was also performed on the CMS images, but without much effect.

On the lower–left image, CMS undersampling has been dimished, but a Moiré pattern can still be detected. See the Web page `http://www.dgp.toronto.edu/people/JamesStewart` for the actual images, which are of higher quality than could be printed in this paper.

On the lower-right image, it is not possible to distinguish the sectors and a smooth penumbra is exhibited. Again, please see the Web page for much clearer images.

Finally, Figure 9 shows a Martian terrain with the sun above the left horizon. Note the soft shadows.

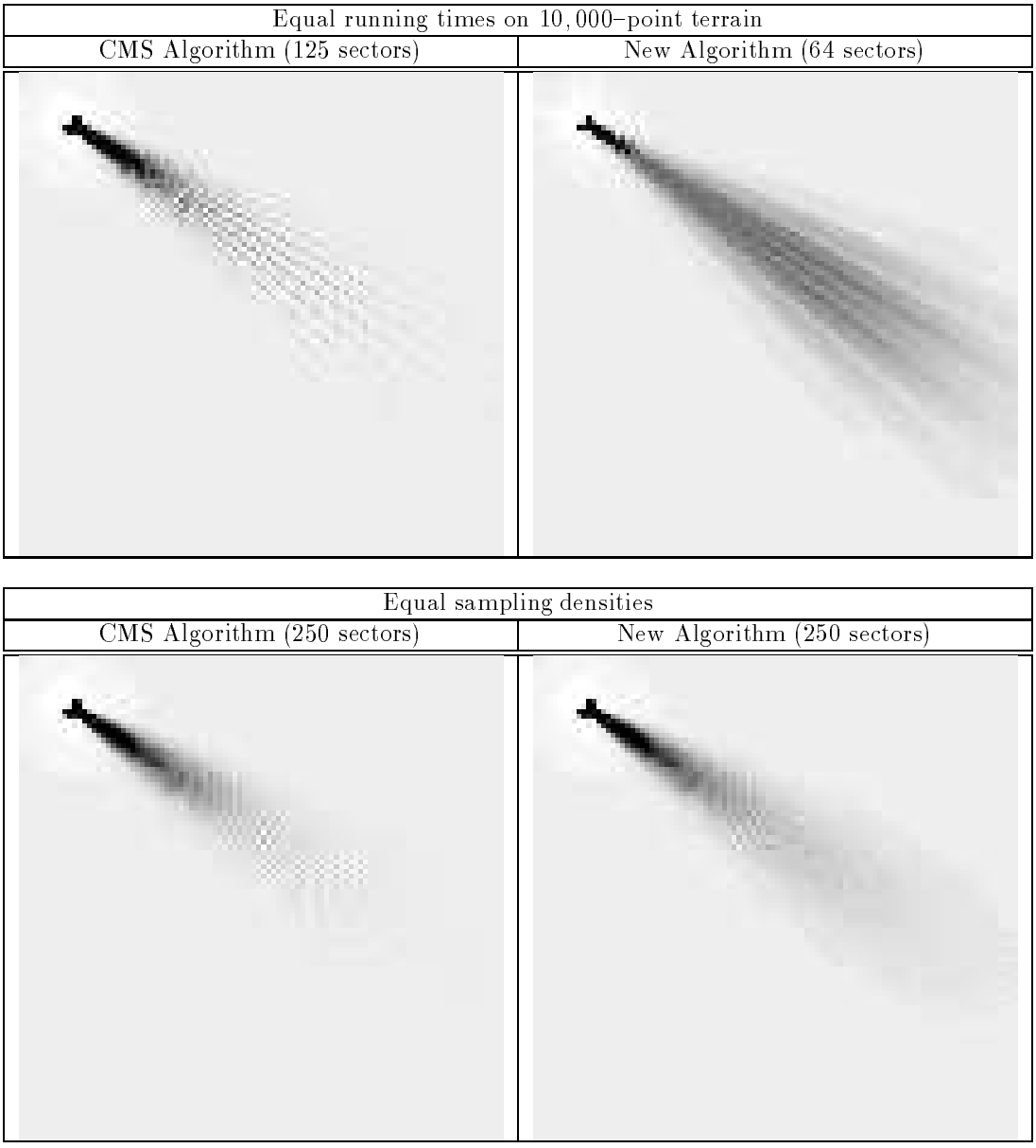

Figure 8: Four images of a flat 10,000–point terrain containing a single spike in the upper–left corner, rendered using horizons computed by the CMS and new algorithms, viewed from directly above. The CMS algorithm misses shadows, especially at low horizon resolutions, while the new algorithm produces smoother penumbras without missing any shadows. Note that the new algorithm will be faster than the CMS algorithm (for the same number of sectors) when the terrain size exceeds 101,000 points.

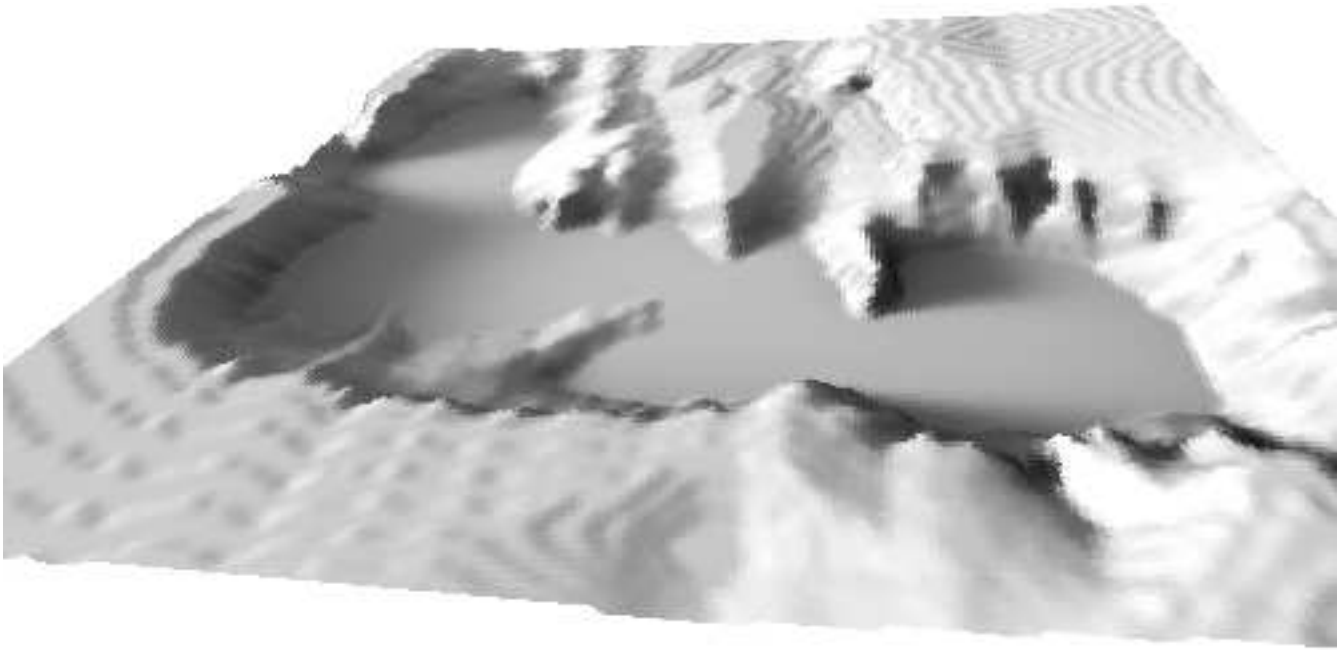

Figure 9: A Martian terrain rendered with the sun 30 degrees above the left horizon. The eight–bit resolution of the height data results in apparent contour lines. Note the soft shadows.

7 Summary

An efficient algorithm has been presented that computes the approximate horizon (consisting of s sectors) at n points of a terrain in time $\mathcal{O}(s\, n \log^2 n)$. The horizons, which only need to be computed once, are used determine the direct primary illumination of each terrain point under any distribution of sky illumination. The direct primary illumination can be used to render the terrain with an approximate radiosity model or can be used as initial input to a progressive radiosity algorithm. The algorithm is easy to implement (only 1100 lines of C++ code).

There are two criteria for evaluating this new algorithm with respect to the existing CMS algorithm: its speed and the quality of images generated from its horizons. The new algorithm is clearly faster than the CMS algorithm, both in experimental and theoretical analysis, once the size of the terrain exceeds about $100,000$ points. Since the execution time of the new algorithm grows more slowly than the CMS algorithm ($\mathcal{O}(n^{1.1})$ versus $\mathcal{O}(n^{1.6})$ in experiments), it becomes even more attractive as the terrain size becomes very large.

Regarding image quality: The new algorithm avoids absent shadows at the risk of introducing spurious shadows. From the images shown, this appears to be a good tradeoff, especially considering that the CMS algorithm will have to take fewer samples in larger terrains to maintain a competitive speed.

I think that the best horizon algorithm would be a blend of the CMS algorithm and the new algorithm. In this "best algorithm," the new algorithm presented in this paper would quickly build a relatively coarse, but complete, horizon for each sample point of the terrain. The CMS algorithm would then refine the horizon in those pairs of adjacent sectors between which a sharp change in elevation is detected. This approach is analogous to that of progressive refinement.

Acknowledgements

The author wishes to thank Mike Caplinger (Malin Space Science Systems) for providing the Mars dataset, and wishes to thank Bob Kanefsky (NASA Ames Research Center) and Doug Obrien (Canada Centre for Remote Sensing) for providing pointers to other datasets.

The Martian terrain data provided by Michael Caplinger of Malin Space Science Systems was processed from the data on the Planetary Data System cd–rom volume MG_2007, "Mars Mosaicked Digital Image Model (MDIM) and Digital Terrain Model (DTM), version 2.0," assembled by Eric Eliason, Raymond Batson, and Anthony Manley.

This cd–rom is available from the National Space Science Data Center, Code 633, Goddard Space Flight Center, Greenbelt, MD 20771.

James Stewart's work is supported by the Information Technology Research Centre of Ontario, the Natural Sciences and Engineering Research Council of Canada, and the University of Toronto.

References

[Ata83] M. J. Atallah. Dynamic computational geometry. In *Proc. 24th Annu. IEEE Sympos. Found. Comput. Sci.*, pages 92–99, 1983.

[Cap] Mike Caplinger. Planetary society marslink project. Technical report, Malin Space Science Systems. available from http://barsoom.msss.com/http/ps/intro.html.

[CG84] Sabine Coquillart and Michael Gangnet. Shaded display of digital maps. *IEEE Computer Graphics and Applications*, 4(7):35–42, July 1984.

[CLR90] T. H. Cormen, C. E. Leiserson, and R. L. Rivest. *Introduction to Algorithms*. The MIT Press, Cambridge, Mass., 1990.

[CMS87] Brian Cabral, Nelson Max, and Rebecca Springmeyer. Bidirectional reflection functions from surface bump maps. In Maureen C. Stone, editor, *Computer Graphics (SIGGRAPH '87 Proceedings)*, volume 21, pages 273–281, July 1987.

[dBD95] Mark de Berg and Katrin Dobrindt. On levels of detail in terrains. In *Proc. 11th Annu. ACM Sympos. Comput. Geom.*, pages C26–C27, 1995.

[DM95] L. De Floriani and P. Magillo. Horizon computation on a hierarchical triangulated terrain model. *Visual Comput.*, 11:134–149, 1995.

[DP88] Leila De Floriani and Enrico Puppo. Constrained Delaunay triangulation for multiresolution surface description. In *Proc. Ninth IEEE International Conference on Pattern Recognition*, pages 566–569, Los Alamitos, California, 1988. CS Press.

[Her89] J. Hershberger. Finding the upper envelope of n line segments in $O(n \log n)$ time. *Inform. Process. Lett.*, 33:169–174, 1989.

[Kaj86] James T. Kajiya. The rendering equation. In David C. Evans and Russell J. Athay, editors, *Computer Graphics (SIGGRAPH '86 Proceedings)*, volume 20, pages 143–150, August 1986.

[KKN+89] Kazufumi Kaneda, Fujiwa Kato, Eihachiro Nakamae, Tomoyuki Nishita, Hideo Tanaka, and Takao Noguchi. Three dimensional terrain modeling and display for environmental assessment. In Jeffrey Lane, editor, *Computer Graphics (SIGGRAPH '89 Proceedings)*, volume 23, pages 207–214, July 1989.

[Max88] Nelson L. Max. Horizon mapping: shadows for bump-mapped surfaces. *The Visual Computer*, 4(2):109–117, July 1988.

[OvL81] M. H. Overmars and J. van Leeuwen. Maintenance of configurations in the plane. *J. Comput. Syst. Sci.*, 23:166–204, 1981.

[PS85] F. P. Preparata and M. I. Shamos. *Computational Geometry: An Introduction*. Springer-Verlag, New York, NY, 1985.

[Rip90] Samuel Rippa. Minimal roughness property of the Delaunay triangulation. *Comput. Aided Geom. Design*, 7:489–497, 1990.

[SL95] A. J. Stewart and M. S. Langer. Towards accurate recovery of shape from shading under diffuse lighting. Technical Report TR-95-162, NEC Research Institute, Princeton, NJ, October 1995.

[SP90] Lori Scarlatos and Theo Pavlidis. Hierarchical triangulation using terrain features. In *Proceedings of the 1st 1990 IEEE Conference on Visualization - Visualization '90*, pages 168–175, IEEE Service Center, Piscataway, NJ, USA (IEEE cat n 90CH2914-0), 1990. IEEE.